# Subsidence Monitoring of Tianjin Suburbs by TerraSAR-X Persistent Scatterers Interferometry

Qingli Luo, Daniele Perissin, Hui Lin, Yuanzhi Zhang, and Wei Wang

***Abstract*—This paper illustrates the first wide area study over Tianjin suburbs of China using persistent scatterers interferometry (PSI) technique for ground subsidence monitoring via high-resolution TerraSAR-X (TSX) SAR data. The deformation rate and the displacement history of the subsiding areas from April 29, 2009 to November 11, 2011 have been reconstructed. The results demonstrate the capability of applying PSI technique to high-resolution SAR time series imageries for monitoring of the subsidence of multiple towns and large-scale man-made linear features (LMLFs) such as railways, highways, and power lines. The comprehensive uncertainties were analyzed between PSI results and ground-leveling data whose densities are very different in both spatial and temporal domains. The overall results show a good agreement with each other. We also found that the underground water extraction and lithological character are the two important potential explanations to the location and shape of the subsiding centers.**

***Index Terms*—Large-scale man-made linear features (LMLFs), multiple towns, persistent scatterers interferometry (PSI), subsidence monitoring, TerraSAR-X, Tianjin suburbs.**

## I. Introduction

GROUND subsidence has always been one of the most severe and widespread geological hazard in cities of China [1]. Most of the monitoring activities are concentrated in urban and downtown areas [2], [3] that have a lesser extent in the suburbs, where specific control points for subsidence monitoring have been implemented. Urbanization in China witnessed numerous large-scale man-made linear features (LMLFs), such as railways, highways, and power lines, connecting the nation as the economic lifelines that are constructed both in urban and suburbs areas, can be seriously jeopardized by the ground deformation. The importance of monitoring deformation along power lines was emphasized especially after the storm hit South China in 2008, which caused thousands of power towers of 110–500 kV transmission lines to be damaged. However, due to the lack of the awareness of the ground subsidence in suburban regions, the potential damages are still underestimated. Consequently, to provide information of land subsidence in suburban areas is urgently needed [4], especially deformation time series, which is able to fill in the blank of motion history in suburban regions that would further provide knowledge for the hazard decision system.

Although traditional leveling and GPS data are able to provide reliable observations of ground subsidence, they are limited by low spatial sampling density and high cost. To overcome these intractable problems, an advanced remote sensing technique, referred to as Differential Interferometric Synthetic Aperture Radar (DInSAR), was introduced as a feasible way to monitor deformation over wide areas with centimeter-to-millimeter accuracy [5]. Furthermore, to overcome the two major limitations of DInSAR, namely spatial/temporal decorrelation and atmospheric disturbance [6], [7], the permanent scatterers (PS) [8], [9] method, known as the first persistent scatterers interferometry (PSI) [10], [11] technique, was suggested as a powerful technique for wide-area deformation monitoring with millimetric precision [12]. Reliable deformation and height correction information can be obtained by adopting stable scattering targets (buildings, structures, etc.) from a long temporal series of interferometric stacks.

In previous investigations [2], significant attention has been focused on studying individual urban area via the PS technique. The reason is that in a general PS analysis, the temporal coherence and spatial density of PS point clusters in an individual downtown area, mostly artificial infrastructures distributed around one cluster center, are usually higher, ensuring the final precision of PS results [9]. However, suburbs often consist of several different towns, each linked to others with roads and distributed in a star-like graph. Thus, it is essential to monitor multiple towns simultaneously and understand the subsiding severity of each town against the background of the entire region without the external ground control points (GCPs) for individuals. Since then, there have been attempts on simultaneous monitoring of urban agglomerations or multiple towns [13]. However, the sparse spatial density of PS points connecting different towns, especially with those medium resolution SAR data, greatly influenced the final precision of PS analysis results, which became an obvious limitation for multi-town PS analysis.

New generations of spaceborne satellites such as TerraSAR-X (TSX) can provide us with high-resolution data and possibly overcome the limitation stated above. The density of PS points extracted from high-resolution SAR data is several times higher than those from medium-resolution SAR data

Manuscript received September 26, 2012; revised January 18, 2013, April 23, 2013, and May 27, 2013; accepted June 02, 2013. This work was partially supported by the Direct Grant (Proj. Ref. No. 2021113), the National Natural Science Foundation of China (NSFC) (Proj. Ref. No. 415911) of HKSAR, and National Natural Science Foundation of China (NSFC) (Proj. Ref. No. 41101370). (*Corresponding author: D. Perissin.*)

Q. Luo, D. Perissin, H. Lin and Y. Zhang are with the Institute of Space and Earth Information Science, The Chinese University of Hong Kong, Hong Kong, China (e-mail: luoqingli2003@163.com; daniele.perissin@cuhk.edu.hk; huilin@cuhk.edu.hk; yuanzhizhang@cuhk.edu.hk).

W. Wang is with the Tianjin Institute of Surveying and Mapping, Tianjin 300381, China (e-mail: wangwei_sgg@163.com).

Color versions of one or more of the figures in this paper are available online at http://ieeexplore.ieee.org.

Digital Object Identifier 10.1109/JSTARS.2013.2271501

[14]. Thus, TSX offers higher temporal coherence of PS pairs with shorter revisit time that would provide better connectivity between towns and further increase the reliability of multitown monitoring. Moreover, high-resolution SAR data have proved to have potential to provide more detailed information when monitoring railways [15], highways, and power lines.

In this paper, we present a first attempt of wide-area analysis in Tianjin suburbs using high-resolution $X$-band SAR data with PS technique that provide simultaneous monitoring of multiple towns and LMLFs, including highways, railways, and power lines. The corresponding validation was done between the PS analysis results over TSX imageries and leveling that will be illustrated and analyzed in detail in the following of presented paper. The work provides a useful guidance and reference for monitoring of star-like-distributed multitowns in suburbs that share a develop pattern similar to Tianjin, as well as monitoring of urban agglomeration. Moreover, the full framework offers a new vision for monitoring of the subsidence of LMLFs.

## II. Study Area and SAR Dataset

The study area is located in the west of Tianjin (see Fig. 2), including the Wuqing District, Jinghai County, and several other towns. Tianjin is located at the junction of the Neocathaysian and the Tianshan-Yinshan (latitudinal) tectonic systems. Huanghua depression is a typical extensional basin that was formed at the intersection of Haihe and Cangdong fault systems.

A dataset of 36 TSX images and 1 Tandem-X (TDX) image (see Table I) are gathered between April 29, 2009 and November 11, 2011 over the Tianjin suburbs. TSX images have a slant range resolution of approximately 3 m for StripMap mode with a wavelength of 3.1 cm and minimum interval of 11 days. The TSX sensor used in this project acquires images along a descending orbit (from North to South) with an incidence angle of approximately 41.08° and ranging 30 by 60 km.

TABLE I
Lists of TSX Images

| Scenes | Date | Perpendicular Baseline (m) | Type | Scenes | Date | Perpendicular Baseline (m) | Type |
|---|---|---|---|---|---|---|---|
| 1 | 20090429 | 12.84 | TSX | 20 | 20091216 | 122.08 | TSX |
| 2 | 20090510 | 30.42 | TSX | 21 | 20091227 | 132.79 | TSX |
| 3 | 20090521 | 64.04 | TSX | 22 | 20100107 | -24.61 | TSX |
| 4 | 20090601 | 42.02 | TSX | 23 | 20100118 | -26.38 | TSX |
| 5 | 20090623 | -77.23 | TSX | 24 | 20100129 | 8.47 | TSX |
| 6 | 20090704 | 18.17 | TSX | 25 | 20100220 | -154.62 | TSX |
| 7 | 20090715 | 34.01 | TSX | 26 | 20100303 | -150.73 | TSX |
| 8 | 20090726 | -112.52 | TSX | 27 | 20100314 | -103.87 | TSX |
| 9 | 20090806 | 137.10 | TSX | 28 | 20100325 | -16.65 | TSX |
| 10 | 20090828 | -101.79 | TSX | 29 | 20100405 | -93.20 | TSX |
| 11 | 20090908 | 40.24 | TSX | 30 | 20100416 | -125.80 | TSX |
| 12 | 20090919 | -64.41 | TSX | 31 | 20100427 | 37.86 | TSX |
| 13 | 20090930 | -181.24 | TSX | 32 | 20100621 | 18.40 | TSX |
| 14 | 20091011 | -43.44 | TSX | 33 | 20100702 | -78.11 | TSX |
| 15 | 20091022 | -65.97 | TSX | 34 | 20100804 | 81.39 | TSX |
| 16 | 20091102 | 118.80 | TSX | 35 | 20100906 | 7.70 | TSX |
| 17* | 20091113 | --- | TSX | 36 | 20101009 | -161.70 | TDX |
| 18 | 20091124 | 46.84 | TSX | 37 | 20101111 | -23.15 | TSX |
| 19 | 20091205 | 125.99 | TSX | | | | |

*: The reference master image.

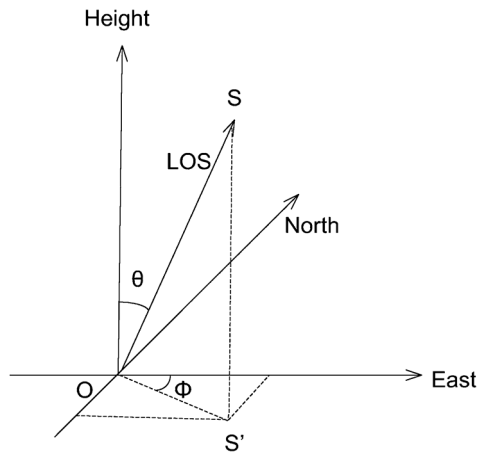


Fig. 1. SAR side-looking geometry and angular parameters.

## III. Methodology

### A. PS Processing

The PS approach was applied to process the available dataset. For a detailed description of the PS approach, please refer to [8], [9], and [16]. The PS analysis requires that at least 25 images are available [8], [9], [16]. All images referring to one common master image were acquired on November 13, 2009. The PS analysis is conducted by the processing software SARPROZ [17]. The applied processing steps are as follows: master image selection, SAR data focusing and registration, baseline construction, digital elevation model (DEM) simulation, differential interferogram generation, persistent scatterers candidate (PSC) selection, multi-image sparse grid phase unwrapping, atmospheric phase screen (APS) estimation and removal [8], [9], [16], PS point selection, PS point displacement history analysis, and average deformation estimation.

DEM from the Shuttle Radar Topography Mission (SRTM) with 3 arc-sec resolution was applied for topographic phase removal. The atmospheric filtering is performed by applying Kriging Interpolation, which uses optimum filtering (removal of outliers) and allows resampling of APS on the regular SAR grid at once [8], [9]. The seasonal oscillation can also be captured by SARPROZ [18]. Most of the results will be displayed overlaid onto the Google Earth (GE). There are two major outputs for each PS analysis: 1) the average velocity map calculated from the entire time period and 2) the displacement time series.

### B. Detected Velocity

SAR side-looking geometry and angular parameters are illustrated in Fig. 1, taking descending pass as an example, where $S$ represents the satellite position and $O$ is the target. The line between satellite and targets gives the Line of Sight (LOS) direction, and $\theta$ is the incidence angle. Dashed line $S'O$ is the projection of $SO$ onto the horizontal plane. $\phi$ is the angle between $S'O$ and the east direction. Thus, the detected velocity along the LOS direction is the geometrical sum of three-dimensional (north–south, west–east and vertical direction) deformation projected to the LOS direction, which is given by [19]

$$\mathrm{disp}_{\mathrm{LOS}} = \underbrace{\sin(\theta)\cos(\phi)\mathrm{E}}_{\mathrm{west-east\ component}} + \underbrace{\sin(\theta)\sin(\phi)\mathrm{N}}_{\mathrm{north-south\ component}} + \underbrace{\cos(\theta)\mathrm{V}}_{\mathrm{vertical\ component}} \quad (1)$$

where E, N, and V are the velocities in west–east, north–south, and vertical direction, respectively.

In our case, $\theta$ is 41.08° and $\phi$ is −10.3°. Thus, (1) can be written as follows:

$$\text{disp}_{\text{LOS}} = \underbrace{0.65\text{E}}_{\text{west}-\text{east component}} - \underbrace{0.12\text{N}}_{\text{north}-\text{south component}} + \underbrace{0.75\text{V}}_{\text{vertical component}} . \quad (2)$$

In (2), given the TSX orbital parameters, the system has a very low sensitivity to the N–S component. Since no other information on the movement direction is available, we assume that the detected movement is mostly vertical. The assumption is supported by previous works, in which GPS study (2006–2010) shows that this area presents a low relative horizontal movement, which could be neglected [20]. Thus, positive velocities detected in our case are simply due to subsiding of the reference point, supported by leveling results.

## IV. Results and Analyses

The average velocity map was derived as illustrated in Fig. 2. More than 940 000 PS points were identified at approximately 522 PS/km$^2$, with the temporal coherence threshold of 0.7. Due to the location of the man-made objects, the spatial distribution of these points is not homogeneous. PS points appear to be populated more densely in residential areas (1,500 ∼ 2,000 PS/km$^2$) compared with agricultural parcels (0 ∼ 10 PS/km$^2$). Significant spatial gaps exist despite of the large number of PS points. As illustrated in Fig. 2, the average velocity ranges from −60 to 20 mm/yr along the LOS direction with respect to (w.r.t.) the reference point (see the pink star), indicating a possible maximum subsidence rate of −80 mm/yr. Red indicates a subsidence rate higher than that of the reference point, whereas blue indicates a subsidence rate lower than the rate of the reference point.

Several subsidence centers of different sizes are shown against the background of large-scale subsidence. Three prime subsidence centers are located in Wangqingtuo Town, Shengfang Town, and Nanhe Town, marked with A, B, and C, respectively, in Fig. 2. Wangqingtuo Town and Shengfang Town have experienced significant subsidence rates ranging from −35 to −60 mm/yr and −30 to −60 mm/yr, respectively, w.r.t. the reference point, whereas the subsidence rate of Nanhe Town is less significant, ranging from −18 to −60 mm/yr. The results highlighted that the strongest activity occurred in Wangqingtuo Town and Shengfang Town. The subsidence rate in Wuqing district and Jinghai district tends to be small and stable compared to those in Xie's study [21]. Nanhe Town is a newly discovered subsidence center with no deformation information from published results. Further investigation is required in that area.

The analysis has been validated by means of eight leveling points provided by the local Institute of Surveying and Mapping. The accuracy of height of the available leveling data has been assessed at 2 mm/km [22].

Before comparing the leveling value and the PS results, the following possible uncertainties were discovered:

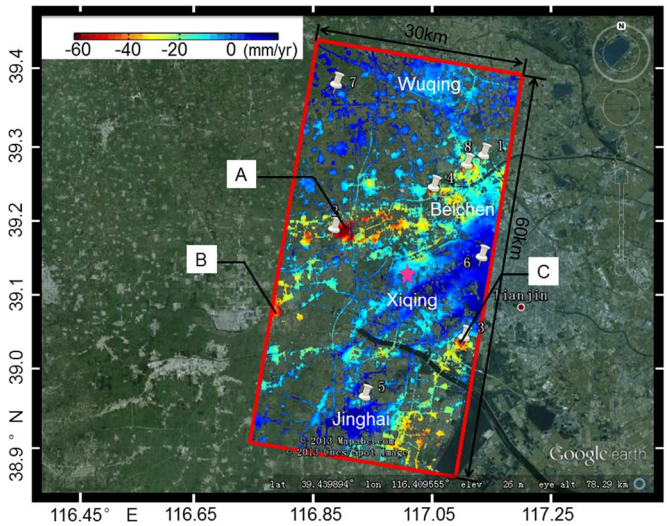


Fig. 2. Linear deformation trend estimated using the PS technique along the LOS direction. The color scale shows stable areas in blue and moving areas in yellow (−30 mm/year) and red (−60 mm/year). The subsidence centers are shown as follows: A is Wangqingtuo Town, B is Shengfang Town, and C is Nanhe Town. The reference point is marked with the pink star. The white placemarks highlight the location of the eight leveling points.

1) The temporal resolution of leveling data is only at the scale of month, while for TSX data the exact acquisition date is available, which leads to a temporal uncertainty of one month regardless of the exact pair of TSX records selected for comparison.
2) The location of the leveling point, released from the data provider, is expected to have an error within 15 m according to handheld GPS measurements. Moreover, horizontal positioning error of PS results cannot be fully neglected, which is introduced by geo-referencing of the PS points used for the comparison. The vertical positioning dispersion can be calculated as a function of the number of images of the dataset $N$, the dispersion of their normal baselines $\sigma_{B_n}$, and the phase noise $\sigma_{\Delta\phi}$ [8], [9], [16], [23]

$$\sigma^2_{\Delta\phi} = \left(\frac{\lambda R_0 \sin\theta}{4\pi}\right)^2 \frac{\sigma^2_{\Delta\phi}}{N\sigma^2_{B_n}} \quad (3)$$

   where $\lambda$ is the wavelength, $\theta$ is the incidence angle, and $R_0$ is the sensor-target distance. For multitemporal data of $N = 37$ images with an incidence angle of $\theta = 0.72$ (41.08°) and a baseline dispersion of $\sigma_{B_n} = 89$ m, a PS with the temporal coherence of $\gamma = 0.8$ ($\gamma \approx e^{-\sigma^2_{\Delta\phi}/2}$ [9], [16]) is localized with an elevation dispersion of about 1.31 m. Thus, a vertical error can be translated into an east–west positioning error of approximately the same size, 1.31 m in the above case.
3) When conducting the PS analysis, the spatial reference point is selected and assumed to be stable in the current study with unknown actual deformation history, which should result in some degree of uncertainty. Moreover, the PS technique measures deformation using "double difference," which will increase the uncertainty.
4) TSX is sensitive along the LOS direction, while leveling measures are only sensitive along a vertical direction.

TABLE II
COMPARISON OF DISPLACEMENT (mm) BETWEEN PS RESULTS AND LEVELING MEASUREMENTS

| ID | Leveling | PS | PS temporal coherence | Dispersion of displacement | PS-Lev | RMSE |
|---|---|---|---|---|---|---|
| 1 | 3.96 | 0.38 | 0.85 | 1.99 | -3.57 | 6.21 |
| 2 | -10.36 | -9.45 | 0.88 | 1.76 | 0.92 | |
| 3 | -24.69 | -20.48 | 0.78 | 2.40 | 4.20 | |
| 4 | -5.84 | -10.56 | 0.95 | 1.12 | -4.72 | |
| 5 | 3.96 | 12.97 | 0.86 | 1.92 | 9.01 | |
| 6 | 21.29 | 24.95 | 0.93 | 1.33 | 3.65 | |
| 7 | 20.54 | 23.39 | 0.94 | 1.23 | 2.85 | |
| 8 | -8.86 | -21.19 | 0.96 | 1.00 | -12.33 | |

During this validation process, no horizontal movement is assumed, which may introduce a certain level of uncertainty. Under this hypothesis, the vertical displacement of leveling measurement is projected into the LOS direction by multiplying $\cos\theta$ ($\theta$ is the incidence angle, 41.08° in this case). The process equals to scaling the measured displacement along the LOS direction by 1.327 $(1/\cos\theta)$, which results in an increase in the estimated root mean square error (RMSE) by a factor of 1.327.

5) Only eight leveling points are available, which is not enough for a statistic point of view. With only a small number of observations, gross error points cannot be eliminated statistically.
6) The reference point for the leveling measurements is assumed to be stable. However, the subsidence of the entire region makes current elevation maps unreliable because the reference point for leveling measurements is most likely subsiding with the entire region, resulting in corresponding uncertainties.

The nearest PS points are selected to compare with the leveling values. The temporal coherence of all eight selected PS points is very high, above 0.85, except for one at 0.78. The dispersion of individual deformation measurements $\sigma_{\text{disp}}$ can be calculated as [16]

$$\sigma_{\text{disp}} = \frac{\lambda}{4\pi}\sqrt{-2\ln(\gamma)} \tag{4}$$

where $\gamma$ is the measured temporal coherence. Then, the dispersion of the difference between two displacements is calculated as $\sigma_{\Delta\text{disp}} = \sqrt{2} * (\lambda/4\pi)\sqrt{-2\ln(\gamma)}$ and listed in Table II, which represents $1 \sim 2$ mm dispersion.

Table II compares the results between PS and leveling. The entire RMSE is 6.21 mm, the minimum difference is 0.92 mm and the maximum difference is $-12.33$ mm. Considering the subsidence rate of this area on a large scale, ranging from $-60$ to 20 mm/yr w.r.t. the reference point setup for the PS analysis, this accuracy may be acceptable. In addressing the uncertainties of the location of the leveling points, ten nearest PS points highlighted with black dots in Fig. 3 are selected for each leveling point. The linear regression is performed between the nearest PS points highlighted with red dots and the leveling points. The correlation coefficient is approximately 0.88, indicating a good agreement between these two distinct measurements.

The subsidence mechanism of the study area was explored with the integration of the geological information. Natural factors and anthropogenic activities are two primary types of causes for the ground subsidence. Anthropogenic activities

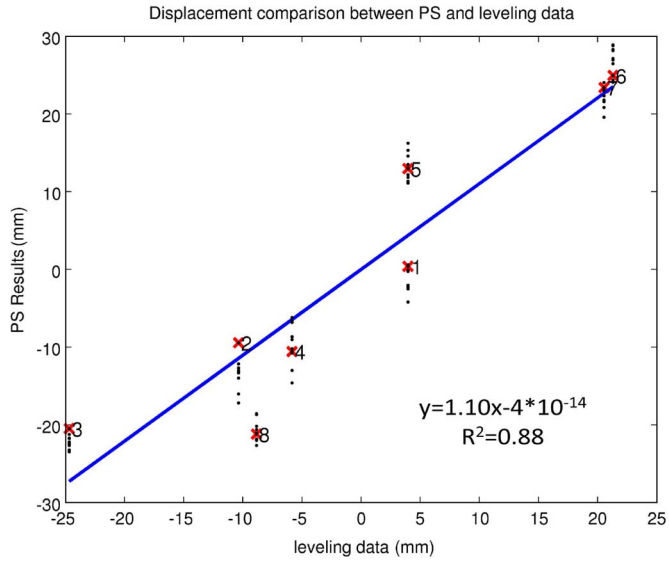


Fig. 3. Displacement comparison between PS and leveling data. There are eight leveling points in total and the ten nearest PS points (black dots) are selected for the comparison. The nearest PS points highlighted with red crosses are used to perform a linear regression (blue line). $X$-axis: leveling data (mm). $Y$-axis: PS results (mm).

have a major contribution to the subsidence, particularly excessive use of underground water resources [24]. However, groundwater withdrawal alone does not result in subsidence centers because of the connectivity of water. To evaluate the geological factors, the PS results and a geological map with a scale of 1:200 000 are geocoded and overlain in GE (see Fig. 4). Most of our study area is covered by quaternary sediments. Alluvium and diluvium, alluvium, marine and alluvium deposit, and lacustrine deposit are four kinds of involved quaternary sediments. The porosity of deposit has effective impact on the degree of ground subsidence when underground water is withdrawn.

In Wangqingtuo town, the surface was formed by alluvial–diluvial, while the surrounding is alluvium and lacustrine deposit. The diameters of dinas in these three sediments decrease successively. Alluvial–diluvial deposit is composed of fine sand and silty sand resulting in high porosity. However, the main component of the other two deposits (alluvium deposit and lacustrine deposit) is clay, and the associated porosity is low. Thus, when the same amount of underground water is withdrawn, subsidence in shallow layer happens more easily in alluvial–diluvial deposit. This could be a good explanation to the severe subsidence in Wangqingtuo Town. Therefore, underground water withdrawal plays a dominant role in the subsidence in Tianjin suburbs. Moreover, other factors, such as lithological patterns, also have impacts on the degree of ground subsidence. For deeper understanding, more investigation and geological materials are required.

## V. DISCUSSION

### A. Monitoring Multiple Towns

With rapid urbanization and industrial development in the suburbs, monitoring multitowns simultaneously in wide ranges

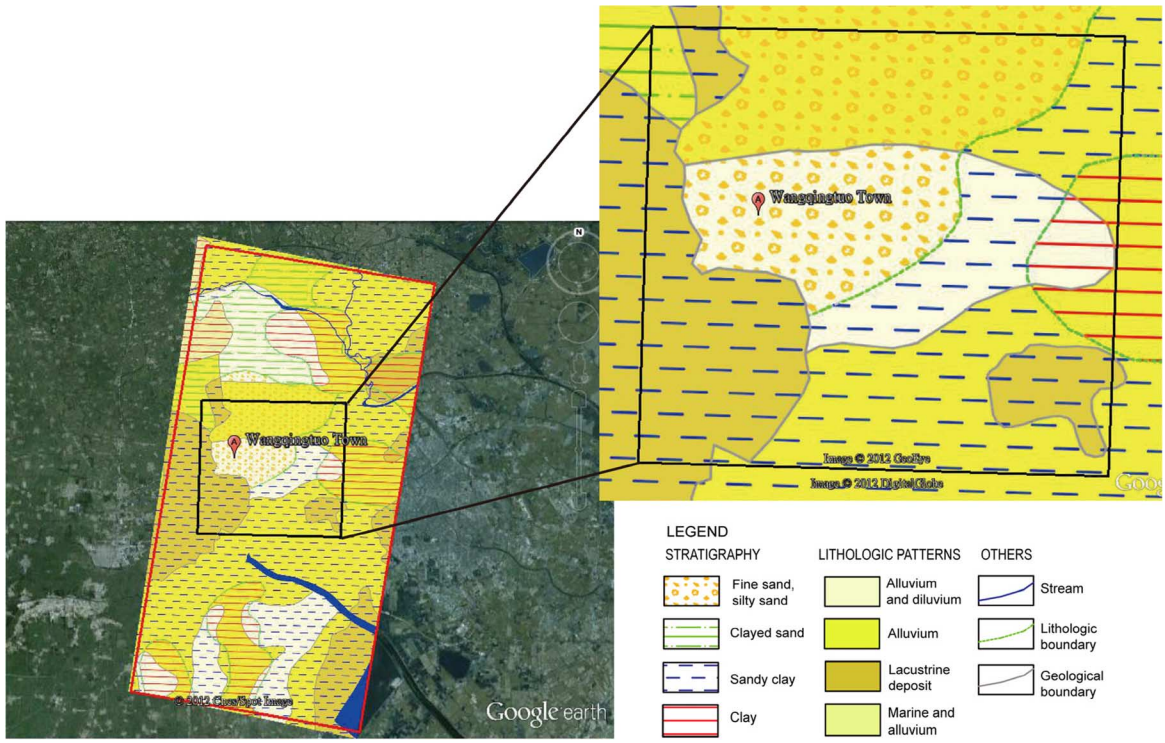


Fig. 4. Geological map with a scale of 1:20 000. The red frame represents the coverage of TSX full frame. The local area around Wangqingtuo Town is framed by the black rectangle which is zoomed in and illustrated in the top right inset. The legend is shown in the lower right corner.

becomes a critical task for monitoring, predicting, and preventing of geological subsidence. Nowadays, with the fast development of high-resolution InSAR satellite system, the above request becomes practical. As shown in Fig. 2, the subsidence over star-like distributed towns referred to one single reference point is clearly displayed, thanks to TSX data and PS technique.

Previous publication [9] has demonstrated that the precision of PS results are related to the accuracy of APS estimation, which depends on the number of available images, the density of PS points, and the reliability of phase difference. In our case, the number of images and density of PS points are already demonstrated to be eligible for the PS analysis; thus, we go further to investigate the reliability of phase difference, a term that is defined by the temporal coherence between two neighboring PS candidates (also called PS pairs), which can be calculated as [8]

$$\gamma = \frac{1}{N}\left|\sum_{i=1}^{N} e^{j\Delta\phi_i}\right| \tag{5}$$

where $N$ represents the number of interferograms and $\Delta\phi_i$ is the phase difference between two neighboring PS candidates of `ith` differential interferogram.

The temporal coherence of the PS pairs in our study area is illustrated in Fig. 5. The network represents the sparse grid of PS candidates used for APS estimation, while the two neighboring PS candidates are connected via lines, for which the color represents the temporal coherence of the PS pairs ranging from 0 (blue) to 1 (red), where 1 indicates the best coherence.

Before analyzing the results, we would like to stress two points [8]: 1) in areas with low PS density where few identifiable PS points can be found, large gaps will exist, and 2) during the process, PS pairs are discarded when $\gamma < \gamma_0$, where $\gamma_0$ ($\gamma_0 = 0.7$) is set as minimum threshold. For a star-like distribution, if the study area is fragmented into different clusters of PS and no reliable equation is available between them ($\gamma < \gamma_0$), the method can only apply to each individual cluster [8], and the external GCPs will be required to connect different clusters.

As illustrated in Fig. 5, the density of PS candidates is high enough (over 635/km$^2$), and meanwhile the temporal coherence of most PS pairs is good. Most important, different towns are connected with relatively high temporal coherence, or what we called a "good connectivity." As shown in the right inset of Fig. 5, Wangqingtuo Town (A) and Donggugang Town (F), 5 km away from each other, were selected for further interpretation. Despite the fact that the two towns are connected via a single road, a lot of PS candidates can be identified along the road due to the high resolution of TSX data. Contrarily, it is never possible to identify enough PS candidates along the roads with medium resolution SAR data [14]. Moreover, the temporal coherence of the PS pairs along this road is close to 1, indicating a superb connection between these two towns. Therefore, with the help of high-resolution SAR data, we are now able to overcome this obstacle of medium resolution SAR data and very much likely to increase the reliability of the PS results without external GCPs.

### *B. Monitoring Highways, Railways and Power Lines*

The high density of PS candidates and good temporal coherence ensure the precision of the results after full-frame TSX PS processing. The average velocity map (see Fig. 2) shows sev-

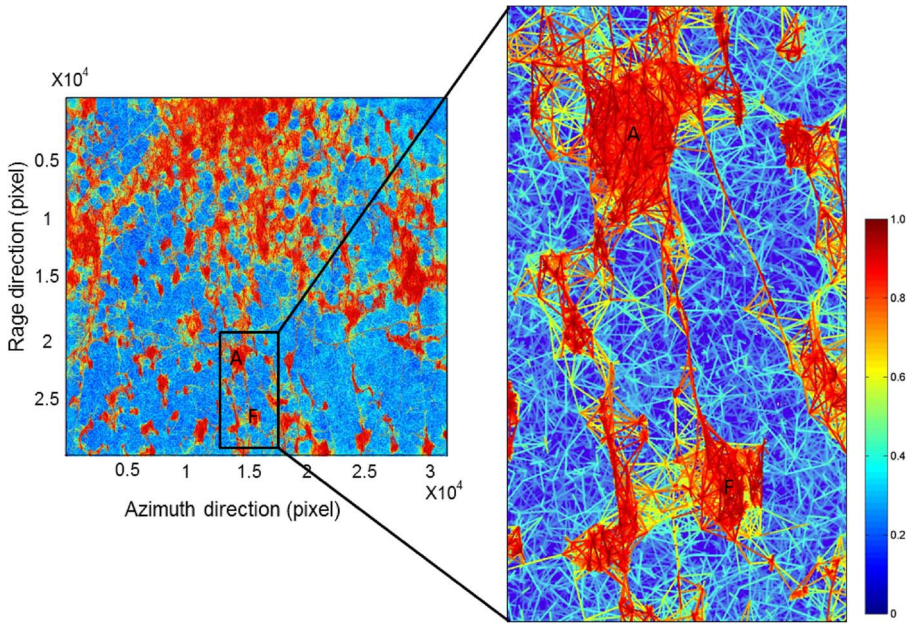


Fig. 5. Sparse grid of PS candidates used for APS estimation and the temporal coherence. $X$-axis: azimuth direction; $Y$-axis: range direction. The color scale shows the temporal coherence ranges from 0 to 1. A: Wangqingtuo Town, F: Donggugang Town.

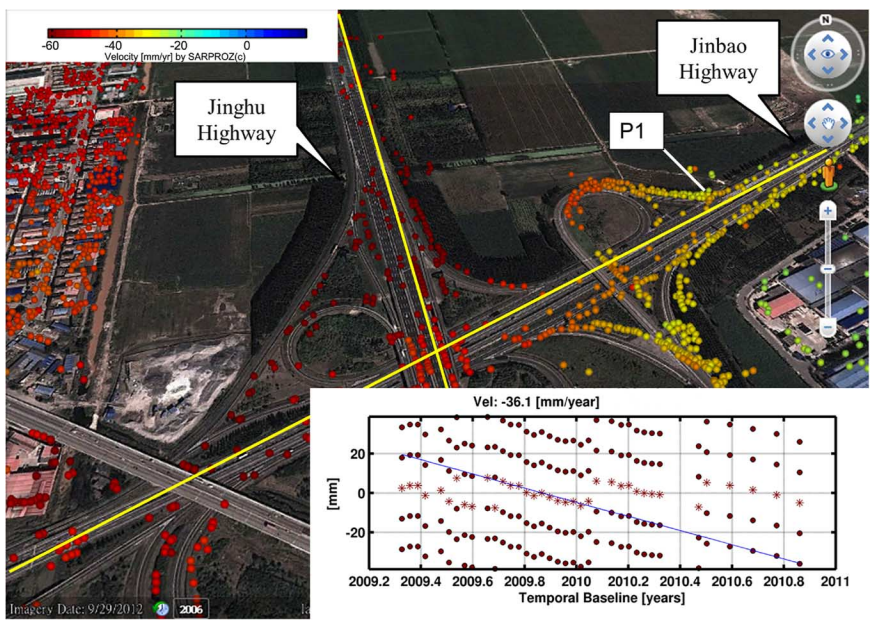


Fig. 6. Two highways across the area around Wangqingtuo Town. The yellow lines highlight Jinghu Highway and Jingbao Highway. P1 gives the location of the selected PS point and its deformation history can be plotted as the figure in the lower right corner. The deformation velocity is presented along the LOS direction. Stars are values between $-\pi$ and $\pi$ (first replica or wrapped values). Dots are adjacent replicas (at $\pm 2k\pi$).

eral criss-crossing lines, identified as highways and railways. This outcome shows that the major traffic network including highway and railway network of entire region can indeed be monitored.

For further understanding, we extracted an area around Wangqingtuo Town, shown in Fig. 6, where two highways highlighted in yellow lines as Jinghu and Jinbao highways intersect with each other. Plenty of PS points were identified along these two highways, and the color scale represents the deformation velocity ranging from $-60 \sim 20$ mm/yr along the LOS direction, w.r.t. the reference point (see the pink star in Fig. 2). Part of Jinghu Highway has suffered subsidence to a maximum subsidence rate of $-60$ mm/yr. One selected PS point (see P1 in Fig. 6) along Jinbao Highway was given its deformation time series with the ambiguous replica of the signal at half the wavelength. Although less TSX acquisitions were received after spring 2010, it is quite clear from the image that there is a linear deformation trend in this area with a continual decline velocity of $-36.1$ mm/yr. The subsidence time series is consistent with the groundwater overexploitation mode [13].

One of the major reasons for the subsidence in this area is underground water withdrawal for the demand of people's

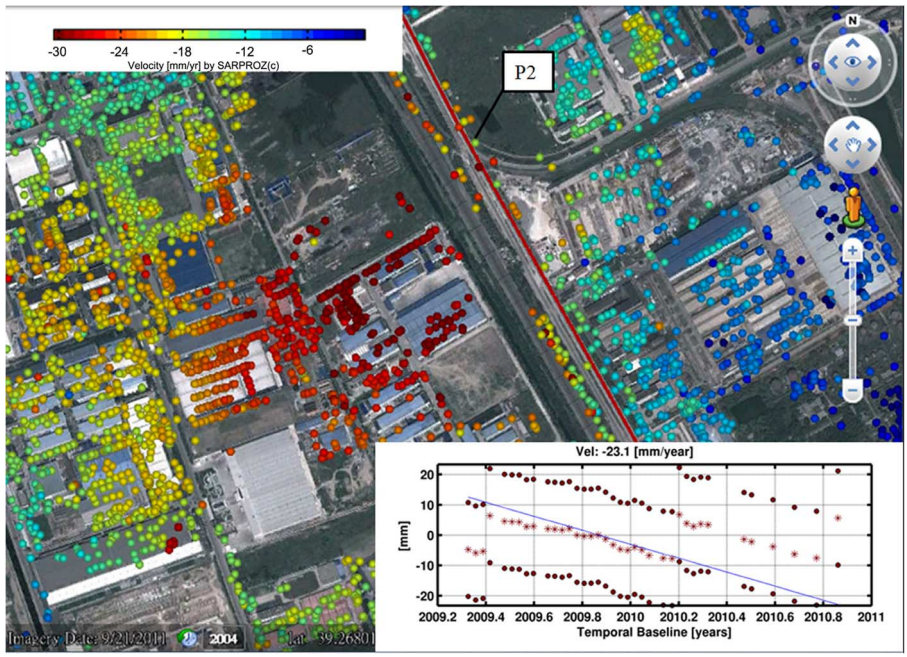


Fig. 7. Jingjin high-speed railway across the area near Shuangjie Town. The red line highlights the railway. P2 gives the location of the selected PS point and its deformation history is displayed in the lower right corner. The deformation velocity is presented along the LOS direction. Stars are values between $-\pi$ and $\pi$ (first replica or wrapped values). Dots are adjacent replicas (at $\pm 2k\pi$).

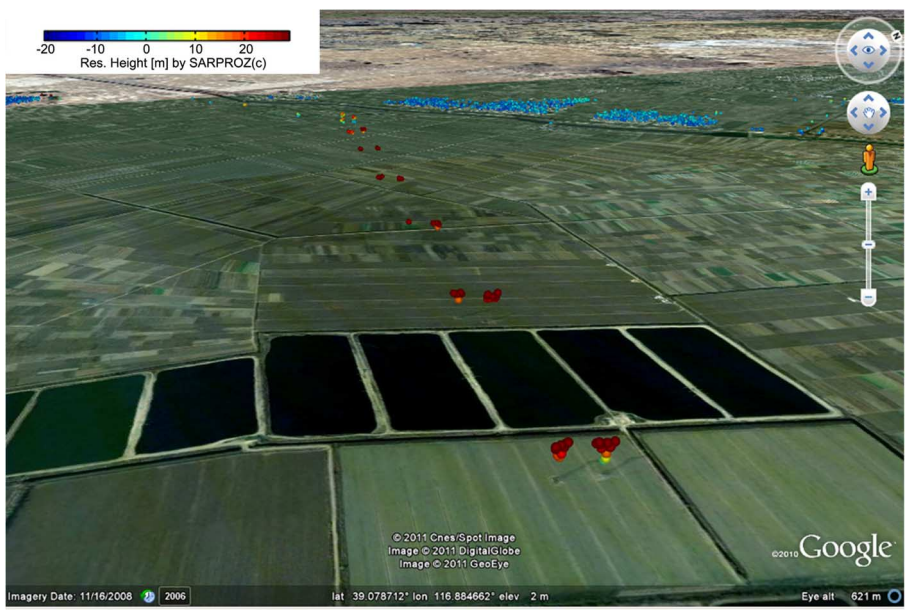


Fig. 8. Power line monitoring by the PS technique with TSX images. The color bar indicates the height of power lines, ranging from $-20$ to 30 m. Using the Google Earth map, the location of power lines can be identified clearly.

daily lives and industry. Another important factor adding to the subsidence may be related to construction dewatering [25]. On a construction site, construction dewatering may be implemented before subsurface excavation for foundations, shoring, or cellar space to lower the water table [25]. The Tianjin Trunk Route of the South-to-North Water Diversion project is across this area. The construction work lasted from July 2009 to May 2011, overlapping with the acquisition time period of SAR data. During that period, construction dewatering was applied and large amount of underground water was exploited, which was sufficient to produce a potential precipitation funnel and cause ground subsidence [26].

Meanwhile, railways have the identical rapid development speed as highways, so are the potential risks. To exploit the potential of TSX data for railway subsidence monitoring, a section of Jingjin High-speed Railway near Shuangjie Town can be extracted as shown in Fig. 7. The railway line was affected by a considerable scale of deformation. The final corresponding displacement time series (referred to a reference belonging to the same area) of one selected PS point marked with P2 is shown in

the lower right corner in Fig. 7. The deformation trend is overall linear despite of slight nonlinear component. Once again, the detail distribution of the railway line was clearly shown by the lining of PS points, indicating that the TSX is capable of providing high PSC density and monitoring railway subsidence. It is also worth mentioning that the railway is crossing two areas that were affected by different deformation rates. One of the important reasons should be different categories of land uses. In Fig. 7, the left bottom side is Beichen economic zones while upper right side is Wuqing agricultural zones. The greater demand of underground water in the industrial area than that in the agricultural areas was a possible explanation for a faster water-level dropping and thus more serious subsidence. It is hence referred that the subsiding trend over the railway region was counteracting and even overlimiting the protection capability of railway foundations.

In addition, it is also important to monitor the movement of power lines and their supports. As opposed to change detection methods [27], our results for power lines monitoring are derived from InSAR time series analysis with high-resolution SAR data. Since the subsidence of power lines in our monitoring region is not so significant, we simply present the height analysis from our PS analysis in Fig. 8 to identify the locations and heights of these power lines supports.

## VI. Conclusion

In this paper, we have performed a first wide area PSI analysis with high resolution $X$-band SAR data covering the Tianjin suburbs (located in the west of Tianjin). A classical PS analysis was applied and three severe subsidence cones were identified from the average deformation map, including one newly discovered subsiding center located in Nanhe Town (see Fig. 2). The results demonstrate that it is feasible to use high resolution SAR data to monitor subsidence jointly over multiple towns (see Fig. 5). The subsidence severity of different towns can be identified clearly without external GCPs by applying the above technique. Shorter revisit period, when coupled with high-resolution TSX, enhances the understanding of subsidence time series. In addition, the possible uncertainties were analyzed in detail between InSAR results and leveling measurements whose spatial and temporal densities are so different. Moreover, the quantitative comparison showed a consistent agreement with a correlation coefficient of 0.88 and a dispersion of 6 mm w.r.t. the given uncertainties (see Fig. 3 and Table II). Those indices were further confirmations of the capability of the TSX data and the applied PS methodology.

By integration of geological materials (see Fig. 4), an excessive amount of groundwater withdrawal is one of the major causes for land subsidence in Tianjin suburbs. Moreover, the lithological character may be another important factor for the formation of subsiding center.

Deformation analysis showed that the PS points along the LMLFs maintain a good coherence even in a relatively long-term time span. The derived annual velocity field covering the Tianjin study site showed that TSX was able to catch impressive motion details and proved its advantages for monitoring LMLFs (see Figs. 6–8), which will be significant for the regional development of China. Furthermore, the linear and nonlinear trend of the subsidence has been detected in the acquisition intervals. The linear subsidence, together with slight nonlinear components, can be detected by the PS technique using a linear deformation model. In addition, when the motion trend is dominated by an evident nonlinear component, a more sophisticated deformation model is suggested to be used for fitting the practical model.

## Acknowledgment

TerraSAR-X data are provided by Infoterra, Germany. The software used in this work is SARProz, developed by D. Perissin. The authors are thankful to data and technical support from the Tianjin Institute of Surveying and Mapping.

## References

[1] Y. Yin *et al.*, "Land subsidence and countermeasures for its prevention in China," *Chin. J. Geologic. Hazard Control*, vol. 16, pp. 1–8, 2005.

[2] D. Perissin and T. Wang, "Time-series InSAR applications over urban areas in China," *IEEE J. Sel. Topics Appl. Remote Sens.*, vol. 4, pp. 92–100, Mar. 2011.

[3] L. Ren *et al.*, "Results of settlement monitoring by GPS in Tianjin during the last ten years," *Sci. Surv. Mapp.*, vol. 31, pp. 17–19, 2006.

[4] T. Li *et al.*, "Ground deformation retrieval using quasi coherent targets DInSAR, with application to suburban area of Tianjin, China," *IEEE J. Sel. Topics Appl. Remote Sens.*, vol. 5, no. 3, pp. 867–873, 2012.

[5] A. K. Gabriel *et al.*, "Mapping small elevation changes over large areas: Differential radar interferometry," *J. Geophys. Res.*, vol. 94, pp. 9183–9191, 1989.

[6] H. A. Zebker and P. Rosen, "Atmospheric artifacts in interferometric SAR surface deformation and topographic maps," *J. Geophys. Res. Solid Earth*, vol. 102, pp. 7547–7563, 1997.

[7] H. A. Zebker and J. Villasenor, "Decorrelation in interferometric radar echoes," *IEEE Trans. Geosci. Remote Sens.*, vol. 30, no. 5, pp. 950–959, 1992.

[8] A. Ferretti *et al.*, "Nonlinear subsidence rate estimation using permanent scatterers in differential SAR interferometry," *IEEE Trans. Geosci. Remote Sens.*, vol. 38, pp. 2202–2212, Sep. 2000.

[9] A. Ferretti *et al.*, "Permanent scatterers in SAR interferometry," *IEEE Trans. Geosci. Remote Sens.*, vol. 39, pp. 8–20, Jan. 2001.

[10] O. Mora *et al.*, "Linear and nonlinear terrain deformation maps from a reduced set of interferometric SAR images," *IEEE Trans. Geosci. Remote Sens.*, vol. 41, no. 10, pp. 2243–2253, 2003.

[11] A. Hooper *et al.*, "A new method for measuring deformation on volcanoes and other natural terrains using InSAR persistent scatterers," *Geophys. Res. Lett.*, vol. 31, pp. 230–234, Dec. 2004.

[12] A. Ferretti *et al.*, "Submillimeter accuracy of InSAR time series: Experimental validation," *IEEE Trans. Geosci. Remote Sens.*, vol. 45, pp. 1142–1153, May 2007.

[13] F. Chen *et al.*, "Ground subsidence geo-hazards induced by rapid urbanization: Implications from InSAR observation and geological analysis," *Nat. Hazards Earth Syst. Sci*, vol. 12, pp. 935–942, 2012.

[14] M. Crosetto *et al.*, "Persistent scatterer interferometry: Potential, limits and initial C-and X-band comparison," *Photogramm. Eng. Remote Sens.*, vol. 76, pp. 1061–1069, 2010.

[15] G. X. Liu *et al.*, "Exploration of subsidence estimation by persistent scatterer InSAR on time series of high resolution TerraSAR-X images," *IEEE J. Sel. Topics Appl. Remote Sens.*, vol. 4, pp. 159–170, Mar. 2011.

[16] C. Colesanti *et al.*, "SAR monitoring of progressive and seasonal ground deformation using the permanent scatterers technique," *IEEE Trans. Geosci. Remote Sens.*, vol. 41, pp. 1685–1701, Jul. 2003.

[17] D. Perissin, "SARPROZ Software Manual," [Online]. Available: http://ihome.cuhk.edu.hk/~b122066/manual/index.html

[18] D. Perissin and F. Rocca, "High-accuracy urban DEM using permanent scatterers," *IEEE Trans. Geosci. Remote Sens.*, vol. 44, pp. 3338–3347, Nov 2006.

[19] D. Massonnet and K. L. Feigl, "Radar interferometry and its application to changes in the Earth's surface," *Rev. Geophys.*, vol. 36, pp. 441–500, 1998.

[20] "Introduction to promote the use of CGCS2000 coordinate system in Tianjin," Tianjin Institute of Surverying and Mapping, Tianjin, China, Internal Tech. Doc., 2011.

[21] D. Xie *et al.*, "Researching on sub-regional management of land subsidence in Tianjin," *Modern Water*, vol. 4, pp. 36–38, 2009.
[22] *Specifications for the First and Second Order Leveling*, China National Standard, 1991.
[23] D. Perissin, "Validation of the submetric accuracy of vertical positioning of PSs in C-band," *IEEE Geosci. Remote Sens. Lett.*, vol. 5, pp. 502–506, Jul. 2008.
[24] K. Dong *et al.*, "Feature of the land subsidence and its damage in Tianjin City," *J. Geologic. Hazards Environ. Preservat.*, vol. 18, pp. 67–70, 2007.
[25] R. T. Ratay, *Handbook of Temporary Structures in Construction: Engineering Standards, Designs, Practices & Procedures*. New York, NY, USA: McGraw-Hill, 1984, pp. (6-2)–(6-9).
[26] Z. Xiao and T. Li, "Effects of Tianjin trunk route of the middle route of South-to-North Water Diversion Project on regional ground water environment," *South-to-North Water Divers. Water Sci. Technol.*, vol. 10, pp. 6–10, 2012.
[27] J. Liu, "Progress in deformation monitoring for dams, bridges and power lines," *Ann. GIS*, vol. 16, pp. 81–90, 2010.

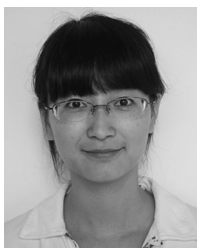

**Qingli Luo** received the M.Eng. degree in photogrammetry and remote sensing from Liaoning Technical University, Fuxin, China, in 2010.

She is currently working toward the Ph.D. degree in SAR inteferometry fields at the Institute of Space and Earth Information Science, The Chinese University of Hong Kong, Hong Kong, China. Her current research interests include subsidence monitoring by applying InSAR and persistent scatterers InSAR techniques.

**Daniele Perissin** was born in Milan, Italy, in 1977. He received the Master's degree in telecommunication engineering and the Ph.D. degree in information technology from the Politecnico di Milano, Milan, Italy, in 2002 and 2006, respectively.

He joined the Signal Processing research group at the Politecnico di Milano in 2002, and since then, he has been working on the permanent scatterers technique (PSInSAR) in the framework of radar remote sensing. Since October 2009, he has held a position as a Research Assistant Professor in the Institute of Space and Earth Information Science (ISEIS) at the Chinese University of Hong Kong (CUHK), where he teaches two courses. He is author of a patent on the use of urban dihedral reflectors for combining multi-sensor Interferometric Synthetic Aperture Radar (InSAR) data, and he has published approximately 80 research works in journals and conference proceedings. He is the developer of the software Sarproz for processing multi-temporal InSAR data.

Dr. Perissin received the IEEE JOURNAL OF SELECTED TOPICS IN APPLIED EARTH OBSERVATIONS AND REMOTE SENSING Best Paper Award in 2012.

**Hui Lin** received the degree from the Wuhan Technical University of Surveying and Mapping, Wuhan, China, in 1980, the M.Sc. degree in cartography and remote sensing from the Chinese Academy of Sciences, Beijing, China, in 1983, and the M.A. and Ph.D. degrees in geographic information systems (GIS) from the University of Buffalo, Buffalo, NY, USA, in 1987 and 1992, respectively.

Since 1993, he has been with The Chinese University of Hong Kong (CUHK), Shatin, Hong Kong, where he is currently a Professor and Director of the Institute of Space and Earth Information Science. His major research interests in satellite remote sensing for cloudy and rainy environment, virtual geographic environments, and historic GIS. He is the Director of the Hong Kong Base of the National Remote Sensing Center of China. He has published over 200 academic papers, coauthored ten books and one atlas, edited ten conference proceedings.

Dr. Lin is the founding President of the International Association of Chinese Professionals in Geographic Information Science (CPGIS) and the Chief Editor of the journal *Annals of GIS*. He was elected an Academician of an International Eurasia Academy of Sciences and member of the Expert Committee of China Lunar Exploring Program in 1995 and 2008, respectively.

**Yuanzhi Zhang** received the Bachelor's degree in geology from the Changchun College of Geology, Jilin University, China; the Master's of Science in remote sensing and cartography from the Chinese Academy of Sciences, Beijing, China; the Master's of Science in remote sensing and geological survey from the International Institute for Geo-Information Science and Earth Observation (ITC), The Netherlands; and the Doctor of Science in technology from the Helsinki University of Technology, Finland.

He joined the Institute of Space and Earth Information Science, the Chinese University of Hong Kong, in October 2006. His research interests include coastal zone studies, land use and cover change detection, water quality and coral ecosystem monitoring, urban heat island effect, and geothermal exploration using remote sensing data.

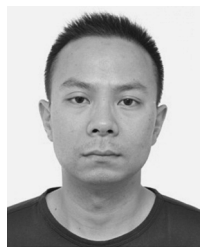

**Wei Wang** received the Ph.D. degree in geodesy and survey engineering from the School of Geodesy and Geomatics (SGG), Wuhan University, China, in 2008.

He is currently working on the GNSS algorithms and applications at the R&D Center of Tianjin Institute of Surveying and Mapping (TJISM), Tianjin, China, where he has held a position as the Deputy Chief Engineer of the R&D Center since September 2012, and he is responsible for algorithm development. His current research interests focus on precise point positioning both in real-time and post-time and continuously operating reference station (CORS) network data processing.